Fluorescencedetected wave packet interferometry. II. Role of rotations and determination of the susceptibility

N. F. Scherer, A. Matro, L. D. Ziegler, M. Du, R. J. Carlson, J. A. Cina, and G. R. Fleming

Citation: The Journal of Chemical Physics **96**, 4180 (1992); doi: 10.1063/1.462837
View online: http://dx.doi.org/10.1063/1.462837
View Table of Contents: http://scitation.aip.org/content/aip/journal/jcp/96/6?ver=pdfcov
Published by the AIP Publishing

Fluorescence-detected wave packet interferometry. II. Role of rotations and determination of the susceptibility

N. F. Scherer,[a] A. Matro, L. D. Ziegler,[b] M. Du, R. J. Carlson,[c] J. A. Cina,[d] and G. R. Fleming

Department of Chemistry and The James Franck Institute, The University of Chicago, Chicago, Illinois 60637

(Received 11 October 1991; accepted 3 December 1991)

The recently developed technique of time-resolved spectroscopy with phase-locked optical pulse pairs is further explored with additional experimental data and more detailed comparison to theory. This spectroscopic method is sensitive to the overall phase evolution of an optically prepared nuclear wave packet. The phase locking scheme, demonstrated for the $B \leftarrow X$ transition of gas phase molecular iodine, is extended through the use of in-quadrature locked pulses and by examination of the dispersed fluorescence signal. The excited state population following the interaction with both pulses is detected as the resultant two-field-dependent fluorescence emission from the B state. The observed signals have periodically recurring features that result from rovibrational wave packet dynamics of the molecule on the excited state electronic potential energy curve. Quantum interference effects cause the magnitude and sign of the periodic features to be strongly modulated. The two-pulse phase-locked interferograms are interpreted with first order time-dependent perturbation theory. Excellent agreement is found between the experimental interferograms and those calculated from literature values of the parameters governing the electronic, vibrational and rotational structure of I_2. A relationship between the phase-locked interferograms and the time-dependent linear susceptibility is obtained. The in-phase and in-quadrature phase-locked interferograms together provide a complete record of the optical free induction decay. Thus by combining the in-phase and in-quadrature data, we obtain the contributions to both the absorptive and dispersive linear susceptibilities arising from transitions within the pulse spectrum.

I. INTRODUCTION

The ability to control the relative optical phase of ultrashort light pulses,[1] as well as their duration and time delay,[2,3] offers new capabilities for the study and manipulation of molecular responses. We have recently reported a new experimental method for setting and maintaining the relative optical phases within a sequence of ultrashort light pulses. [Ref. 1, referred to here as I] The time and frequency integrated spontaneous resonance emission of I_2 vapor excited by a pair of phase-controlled pulses, monitored as a function of the inter-pulse time delay, exhibited periodic oscillations and decay. Because of phase locking, the frequency of oscillation of the two-pulse interference is reduced from the optical (i.e., electronic) to the vibrational domain. It was shown in paper I[1] that the fluorescence interferogram records the quantum mechanical interference between the two excited state nuclear wave packets prepared by the pulse pair as the interference contribution to the excited state population. The wave packet prepared by the initial pulse propagates on the upper potential surface during the interpulse delay, while the reference wave packet originates from a stationary ground state wave function. It was found that the fluorescence-detected interferences are absent when control over the relative optical phase of the pulses is not actively maintained. Interference signals were observed for time delays three orders of magnitude longer than the pulse duration.

The interval between recurrences in the interference contribution to the B-state population of I_2 corresponds to the inverse of the excited state vibrational level spacing. Paper I compared experimental interferograms with interferograms calculated when only the vibronic levels of I_2 are included (i.e., nonrotating I_2). The vibronic model calculations correctly accounted for the periodic return of the initially prepared wave packet to the Franck–Condon region, which is necessary for interference with the reference wave packet generated by the delayed pulse. Qualitative agreement was found in the delay times for maximum constructive and destructive interference. The overall form of the fluorescence interferogram varied greatly with changes in the frequency of the selected spectral components of the pulse pair, termed the locked frequency, between which a constant phase angle was maintained. The dependence of the form of the interferogram on the locked frequency was shown to be a consequence of the fact that the interference contribution to the excited state population of a given vibronic level is governed by the difference between the locked frequency and the transition frequency to that level.

Despite the qualitative agreement between many features of the observed and calculated interferograms, significant differences remained. In particular, the observed inter-

[a] National Science Foundation Postdoctoral Fellow.
[b] Permanent address: Department of Chemistry, Boston University, Boston, Massachusetts 02215.
[c] Deceased.
[d] Camille and Henry Dreyfus Teacher–Scholar.

 0021-9606/92/064180-15$06.00

ference signal exhibited a more pronounced decrease in amplitude with interpulse delay than obtained in the vibrations-only calculations. One of the purposes of this paper is to investigate the effects of the rotational level structure on the interference signal. We show that the proper inclusion of rotational as well as vibronic structure captures the observed decay of the interference amplitude. In addition, it is found that an accurate treatment of the single pulse intensity spectrum is necessary for quantitative agreement with experiment.

Resonant[4–7] and nonresonant[8,9] femtosecond pump–probe studies in both liquid[4,5,7–9] and gaseous[6] media often exhibit impulsively excited vibrational oscillations which decay, in general, due to both homogeneous and inhomogeneous dephasing mechanisms.[10,11] These pump-induced nuclear responses correspond to the decay of vibrational coherences on the ground and/or excited electronic state potential energy surface. For such electronically resonant experiments, interference contributions to the excited state responses due to the phase evolution of initially prepared vibronic coherences result only during the duration of the pump pulse.[12,13] In contrast, the damped oscillations reported here arise from the rovibronic wave packet evolution during the time interval between the two excitation fields referenced to a near-resonant (i.e., locked) frequency. As shown below, these oscillatory interference features are damped by homogeneous and inhomogeneous mechanisms related to electronic coherences. The phase-locked fields prepare (pump) the vibronic coherence and probe the time evolution of the subsequent linear polarization for time delays long compared to the pulse duration. The evolution of ultrashort-pulse-prepared vibronic coherences are also probed in photon echo experiments,[10–12] but without sensitivity to the phase of the induced polarization.

Theoretical studies of the effects of excitation with two or more pulses of well defined inter-pulse phase relationship have been reported by Villaeys and Freed[14] and Metiu and Engel.[15] The latter authors investigated the effects of pulse pair phase on the yield in one-photon two-pulse photodissociation of NaI. Metiu and Engel also discussed the analogy of phase-locked pulse pair excitation to experiments exhibiting spatial interference such as Young's double-slit experiment. Some discussion of the optical phase dependent interference effects in molecular electronic transitions has been given by Tannor, Rice, and co-workers,[16] though the main emphasis of their studies has been the possible use of the delay between pulses of different color to control the two photon-induced chemical reaction products.

Romero-Rochin and Cina recently investigated the possible use of phase-controlled optical pulses to monitor electronic geometric (i.e., Berry) phase evolution in Jahn–Teller systems.[17] In the experiments suggested by these authors, molecular pseudorotation in a nondegenerate electronic ground state would be driven by a nonresonant impulsive Raman process. Transitions to a Jahn–Teller active excited electronic state would then be produced with a pair of resonant phase-locked pulses. In the limiting case of weak electronic-nuclear coupling, the inter-pulse delay dependence of the interference contribution to the excited state population is predicted to manifest electronic geometric phase development through oscillation at twice the pseudorotational period.

In this paper, we report additional experimental studies of fluorescence-detected wave packet interferometry in I_2 vapor as well as more detailed calculations of these signals. Section II briefly reviews the experimental approach. The origin of the interference signal is then described (in Sec. III) with a first order time-dependent perturbation theory calculation of the excited state population arising from a resonant composite pulse. An analysis of the relationship between the phase-controlled interferograms and the frequency-dependent absorptive and dispersive susceptibilities is also given. Section IV presents and compares the experimental and calculated interferograms. As mentioned above, it is found that inclusion of the rotational degrees of freedom accounts for the observed decrease in the magnitude of the recurrence features with increasing delay between pulses. The in-phase and in-quadrature interferograms are combined, according to the prescription of the theoretical section, yielding the absorptive and dispersive contributions to the linear susceptibility arising from resonant transitions between the X and B states. This result emphasizes the relationship of ultrafast spectroscopy with phase-locked pulses to previous time-dependent approaches to the calculation of continuous-wave spectra.[18–22] Finally, interferograms obtained with dispersed fluorescence detection at several emission wavelengths and for variable spectral bandpasses are reported and analyzed. A discussion is given in Sec. V along with concluding remarks.

It should be mentioned that, in a very recent report, Bavli, Engel, and Metiu[23] present theoretical calculations similar to those of paper I, but including rotational structure, as is done here. They illustrate the sensitivity of phase-locked spectroscopy to the B-state potential surface of iodine and contrast these results with two-color pump–probe spectroscopy.[6] Although a detailed comparison with the experimental results is not given, Metiu and co-workers corroborate the conclusion that the rotational level structure accounts for the overall decay of the interference signal in these room temperature experiments.

II. EXPERIMENT

The experimental system has been described in detail in paper I and will only be briefly summarized here. The laser system consists of a mode locked Nd:YAG laser, an antiresonant ring dye laser, a regenerative amplifier and a dye amplifier. The frequency doubled pulse train of the YAG laser is used to pump the antiresonant ring dye laser. The dye laser is cavity dumped at a repetition rate of 500 kHz and the pulses are nominally 50–60 fs Gaussian FWHM in duration. The mechanism of pulse formation is characteristic of a colliding pulse mode locked dye laser which can be adjusted to operate in a regime described by soliton pulse shaping.[24] The intensity spectrum of the cavity dumped pulses is recorded and used for the comparison of theory and experiment. Unamplified pulses from the dye laser are used directly in the case of the total emission measurements.

Due to the small absorbance of the sample, the dispersed emission studies require greater photon flux to achieve reasonable ($\sim$2 h) signal averaging times. The pulse amplification occurs as follows. A portion of the 1.064 μm fundamental of the YAG oscillator is directed to the regenerative amplifier and a single pulse is acousto-optically diffracted into the second YAG cavity. After approximately 120 round trips the amplified pulse is diffracted out and frequency doubled. The injection and extraction is done at a repetition rate of 100 kHz.[25] The second harmonic beam is split into two optical delay lines and used to pump a two-stage dye amplifier with a 1.25 mm thick dye jet gain medium. The cavity dumper of the femtosecond pulse dye laser is electronically synchronized with the cavity dumper of the regenerative amplifier. The dye laser pulses are optically delayed and aligned collinearly but counterpropagating with the 532 nm pump beam through the dye jet to obtain optimal gain extraction without saturation.[26] The pulses from the dye laser are amplified more than 50-fold to 150 nJ energies but retain the 50–60 fs pulse duration.

The femtosecond pulses are entrant on an optically stabilized Michelson interferometer. A double slot mechanical chopper amplitude modulates each beam within the interferometer. The beams from the interferometer are recombined collinearly, focused through a 100 μm pinhole using a spherical mirror, and recollimated with another spherical mirror. The combined beams are split such that 90% of the light intensity is directed into the I_2 gas cell and 10% is f-number matched via two achromat lenses into a 0.34 m monochromator. Fluorescence emission from the gas cell is collected in a right angle geometry and imaged with 1.5:1 magnification onto a photomultiplier tube. The electrical signal is processed in a lock-in amplifier and is referenced to the double amplitude modulation of the two optical beams in the interferometer. The signal is recorded following discrete steps of the delay line.

Phase locking for time separated femtosecond pulses relies on the detection of electric field interference accomplished by the temporal dispersion of the pulses following propagation through a monochromator.[1] The electric field interference of the pulses that are geometrically broadened in the monochromator can be detected for time separations less than the inverse of the monochromator resolution, presently 0.67 cm^{-1}, or about 25 ps, corresponding here to delays nearly 3 orders of magnitude greater than the pulse durations. The detected intensity of this bandpass is processed in a second lock-in amplifier. This second lock-in amplifier is referenced to the sinusoidal modulation applied to a piezoelectric transducer (PZT) supporting the end mirror of one arm of the interferometer. The amplitude of the mirror displacement is approximately 60 nm ($\lambda/10$ at $\lambda = 610$ nm). The output of the second lock-in amplifier is used as an error signal to adjust the relative lengths of the two arms of the interferometer, and hence the phase difference of the two pulses for the selected spectral component of the pulses. The relative phase angle of the common locked frequency component of the two pulses is maintained at $2n\pi$, $(2n+1)\pi$ or $(2n \pm 1/2)\pi$ for in-phase, out-of-phase, and in-quadrature pulses, respectively, for integral values of n. All wavelengths reported below have been corrected for the refractive index of air. The sample cell contained I_2 vapor at room temperature, 360 mTorr pressure, and an extinction coefficient of $\epsilon = 44\ \ell\,mol^{-1}\,cm^{-1}$ at 610 nm. This wavelength is on the red edge of the $B \leftarrow X$ absorption profile.

III. THEORETICAL

A. Interference signal including rotations

Several features of the experimental I_2 interference signal were clarified by displaced harmonic and anharmonic oscillator model calculations in paper I. It was shown that the return of the initially prepared wave packet to the Franck–Condon region accounts for the observed extrema of the interference signal with the $\sim$300 fs interval corresponding to the B-state vibrational period. In addition, the crossover from positive-going recurrences, manifesting constructive interference, to negative-going peaks, resulting from destructive interference, was found to depend on the difference between the locked frequency and the frequency of the nearest vibronic transition. Slight shifts in the interference peak positions away from the precise return time to the Franck–Condon region were shown to result from compromises between maximal spatial overlap of the propagated and reference wave packets, on one hand, and optimal overall phase-matching between them, on the other.

The calculations of paper I did not include rotational structure and assumed a Gaussian pulse shape. Here we incorporate the rotational contributions to the transition energies, apply angular momentum selection rules appropriate to the $B \leftarrow X$ transition,[27] and use the experimentally determined pulse shapes. It is demonstrated below that the rapid decay of the interference amplitude, the main feature not accounted for by the vibrations-only calculations, is primarily a consequence of the thermal occupation of many ground state rotational levels and the difference in rotational constants between the X and B states.

We use first order time-dependent perturbation theory to calculate the interference contribution to the excited state population of a diatomic molecule. The expression we obtain is essentially similar to Eq. (4.42) in paper I, except that here we explicitly include the rotational sublevels. The Hamiltonian has the form

$$H = |g\rangle H_g \langle g| + |e\rangle H_e \langle e|, \tag{3.1}$$

where g and e denote ground and excited electronic states, respectively, and H_e and H_g are the corresponding nuclear Hamiltonians. The interaction with the laser is given in the dipole approximation by

$$V(t) = -\boldsymbol{\mu}\cdot\mathscr{E}(t), \tag{3.2}$$

where $\boldsymbol{\mu}$ is the dipole moment operator which connects $|g\rangle$ and $|e\rangle$, and $\mathscr{E}(t)$ is the electric field. For the $B \leftarrow X$ transition, which is parallel with the internuclear axis, the interaction becomes

$$V(t) = -\mu\mathscr{E}(t)\cos\theta, \tag{3.3}$$

where θ is the angle between the polarization direction of the field and the internuclear axis. In the present experiments, $\mathscr{E}(t)$ has the form

$$\mathscr{E}(t) = \mathscr{E}_1(t) + \mathscr{E}_2(t), \tag{3.4}$$

where

$$\mathscr{E}_1(t) = E(t)\cos[\Omega t] \tag{3.5}$$

and

$$\mathscr{E}_2(t) = E(t-t_d)\cos[\Omega(t-t_d) + \Omega_L t_d + \phi]. \tag{3.6}$$

$E(t)$ is the envelope of the laser pulses, Ω is the carrier frequency, Ω_L is the locked frequency, t_d is the delay time between the pulses, and ϕ is the phase-locking angle.

Starting in the rovibrational level $|v''(J'')\rangle|J''M''\rangle$, of the electronic ground state, the excited state rovibrational wave function prepared by the composite pulse (3.4) becomes

$$\begin{aligned}\langle e|\Psi(t)\rangle = i\mu_{eg} \sum_{J'=0}^{\infty} \sum_{M'=-J'}^{J'} \sum_{v'} |v'(J')\rangle|J'M'\rangle \\ \times \exp(-i\epsilon_{v',J'}t)\langle v'(J')|v''(J'')\rangle \\ \times \langle J'M'|\cos\theta\,|J''M''\rangle \\ \times \int_{-\infty}^{\infty} d\tau \exp[i(\epsilon_{v',J'} - \epsilon_{v'',J''})\tau] \\ \times [\mathscr{E}_1(\tau) + \mathscr{E}_2(\tau)].\end{aligned} \tag{3.7}$$

We have taken $\hbar = 1$.

Calculating $|\langle e|\Psi(t)\rangle|^2$ yields the excited state population. We are interested in the contribution due to interference between the separate wave packets prepared by $\mathscr{E}_1$ and $\mathscr{E}_2$. Taking μ_{eg} to be real and expressing the integral in Eq. (3.7) in terms of the Fourier components of $\mathscr{E}_1$ and $\mathscr{E}_2$ gives an interference contribution of

$$\begin{aligned}P^{\text{int}}_{(v'',J'',M'')}(t_d) = 4\pi\mu_{eg}^2 \sum_{v'} \Bigg\{\Bigg[|\langle v'(J''+1)|v''(J'')\rangle|^2 \left(\frac{(J''+M''+1)(J''-M''+1)}{(2J''+1)(2J''+3)}\right) \\ \times \mathrm{Re}\{\mathscr{E}_1(\epsilon_{v',J''+1} - \epsilon_{v'',J''})\mathscr{E}_2^*(\epsilon_{v',J''+1} - \epsilon_{v'',J''})\}\Bigg] + \Bigg[|\langle v'(J''-1)|v''(J'')\rangle|^2 \\ \cdot \left(\frac{(J''+M'')(J''-M'')}{(2J''+1)(2J''-1)}\right) \mathrm{Re}\{\mathscr{E}_1(\epsilon_{v',J''-1} - \epsilon_{v'',J''})\mathscr{E}_2^*(\epsilon_{v',J''-1} - \epsilon_{v'',J''})\}\Bigg]\Bigg\}.\end{aligned} \tag{3.8}$$

Since the sample is initially in equilibrium, with no coherence among ground state rovibrational levels, the observed interference signal is given by a sum over the $P^{\text{int}}_{(v'',J'',M'')}$ with thermal weighting

$$P^{\text{int}}(t_d) = \frac{1}{Z} \sum_{v'',J'',M''} e^{-\beta\epsilon_{v'',J''}} P^{\text{int}}_{(v'',J'',M'')}(t_d), \tag{3.9}$$

where Z is the partition function. Performing the sum over M'', Eq. (3.9) simplifies to

$$P^{\text{int}}(t_d) = \frac{1}{Z} \sum_{v'',J''} e^{-\beta\epsilon_{v'',J''}} P^{\text{int}}_{(v'',J'')}(t_d) \tag{3.10}$$

with

$$\begin{aligned}P^{\text{int}}_{(v'',J'')}(t_d) = 4\pi\mu_{eg}^2 \sum_{v'} \Bigg(\Bigg\{|\langle v'(J''+1)|v''(J'')\rangle|^2 \frac{J''+1}{3} |\mathscr{E}_1(\epsilon_{v',J''+1} - \epsilon_{v'',J''})|^2 \\ \times \cos[(\epsilon_{v',J''+1} - \epsilon_{v'',J''} - \Omega_L)t_d - \phi]\Bigg\} + \Bigg\{|\langle v'(J''-1)|v''(J'')\rangle|^2 \frac{J''}{3} \\ \times |\mathscr{E}_1(\epsilon_{v',J''-1} - \epsilon_{v'',J''})|^2 \cos[(\epsilon_{v',J''-1} - \epsilon_{v'',J''} - \Omega_L)t_d - \phi]\Bigg\}\Bigg).\end{aligned} \tag{3.11}$$

In Eq. (3.11) we have used the relationship

$$\mathscr{E}_2(\xi) = \mathscr{E}_1(\xi)\exp[i(\xi - \Omega_L)t_d - i\phi)] \tag{3.12}$$

between components of the phase-locked pulses.

In the derivation of the interference signal (3.10) and (3.11) as the interference contribution to the excited state population, it has been tacitly assumed that the radiative lifetimes of the excited vibronic states greatly exceed the longest delay between the pulses and that the molecules are otherwise isolated on the time scale of the excitation process. Both of these assumptions are justified for iodine vapor under the conditions of the experiments described below.

B. Linear susceptibility

The experiments reported here and in paper I can be understood as optical free induction decay measurements with sensitivity to the instantaneous phase of the induced linear polarization. Positive and negative interference contributions to the excited state population correspond, respectively, to increases and decreases in the energy of the system because of the interaction of the delayed pulse electric field with the polarization induced by the initial pulse (cf. Appendix A of paper I). Maintenance of a specific phase relationship between the pulses allows determination of the magni-

tude and phase of the induced optical polarization. In terms of the system density matrix, the initially prepared rovibronic coherence can be converted into an increase or decrease in the excited state population depending on the relative phase between it and the delayed-pulse electric field. This point of view is elaborated in the Appendix below.

In this section, we show that the in-phase ($\phi = 0$) and in-quadrature ($\phi = \pi/2$) interferograms can be combined to determine the linear susceptibility governing the optical free induction decay. The determination is complete in the sense that both the real (dispersive) and the imaginary (absorptive) parts of the frequency-dependent linear susceptibility are obtained directly. To keep notation simple, we omit reference to the rotational degrees of freedom in this subsection.

Neglecting rotational terms in Eq. (3.8) and again using Eq. (3.12), the interference contribution to the excited state population from a single ground state vibrational level is

$$P^{\rm int}(t_d) = 4\pi\mu_{eg}^2 \sum_{\nu'} |\langle \nu' | \nu'' \rangle|^2 |\mathscr{E}_1(\epsilon_{\nu'} - \epsilon_{\nu''})|^2 \times \cos[(\epsilon_{\nu'} - \epsilon_{\nu''} - \Omega_L)t_d - \phi]. \quad (3.13)$$

In the limiting case that the pulses are short enough in duration that $|\mathscr{E}_1|^2$ is independent of frequency over the entire absorption spectrum, the general expression (3.13) reduces to

$$P^{\rm int}(t_d) = 4\pi |\mathscr{E}_1|^2 \mu_{eg}^2 \, {\rm Re}\{\exp[i(\Omega_L + \epsilon_{\nu''})t_d + i\phi] \times \langle \nu'' | \exp(-iH_e t_d) | \nu'' \rangle\} \quad (3.14)$$

[compare Eq. (4.18) of paper I].

We seek the relationship between the signals (3.14) for $\phi = 0$ and $\pi/2$ and the time-dependent dipole susceptibility. The time-dependent susceptibility is related to the time correlation function of the electronic dipole moment operator according to[28]

$$\chi(t) = 2\,{\rm Im}\langle \nu'' | \langle g | \mu(0)\mu(t) | g \rangle | \nu'' \rangle \quad (3.15a)$$

$$= 2\mu_{eg}^2\,{\rm Im}[\exp(-i\epsilon_{\nu''}t)\langle \nu'' | \exp(iH_e t) | \nu'' \rangle], \quad (3.15b)$$

for $t > 0$ and zero otherwise. The overlap function that appears in Eq. (3.15a) is the same type that appears in the time integral expression for the continuous absorption spectrum[29] (cf. Sec. V). Here $\mu(t)$ is the dipole moment operator in the Heisenberg representation. Isolating the imaginary part of the overlap function in Eq. (3.15b) with an appropriate combination of the in-phase and in-quadrature signals, given by Eq. (3.14), leads to

$$\chi(t_d) = \frac{1}{2\pi |\mathscr{E}_1|^2} \{P_0^{\rm int}(t_d) \sin \Omega_L t_d + P_{\pi/2}^{\rm int}(t_d) \cos \Omega_L t_d\}. \quad (3.16)$$

This expression for $\chi(t_d)$ provides complete information on the resonant linear response of the system to an external field, not just to one or the other of the absorptive or dispersive parts. This is the same information one would obtain from a phase sensitive free induction decay measurement.[30] Interestingly, the right-hand side of Eq. (3.16) is explicitly dependent on Ω_L, while the left-hand side, of course, is not. This corresponds to the fact that the information content of the combined in-phase and in-quadrature interferograms is independent of the locked frequency, despite the drastic changes in their appearances with changes in Ω_L.

Unfortunately, the simple expression (3.16) applies only when the pulse width spans the entire absorption spectrum. However, account can be taken of the nonidealities introduced by a more limited pulsewidth. If the laser pulses are not arbitrarily abrupt, one can no longer write down an expression relating $\chi(t_d)$ to the interference contribution to the population; the finite spectral range of the pulses prohibits the complete determination of the system's response. Nonetheless, the contributions to the real and imaginary parts of the frequency-dependent susceptibility within the spectral range of the laser pulses, arising from transitions in that range, can be directly determined.

The frequency-dependent linear susceptibility can be expressed as[28]

$$\chi(\xi) = \chi'(\xi) + i\chi''(\xi), \quad (3.17)$$

where

$$\chi(\xi) = \int_0^\infty dt \exp(i\xi t)\chi(t) \quad (3.18)$$

is the Fourier transform of Eq. (3.15a). For the system we are considering $\chi'(\xi)$ and $\chi''(\xi)$ can then be written as

$$\chi'(\xi) = \mu_{eg}^2 \sum_{\nu'} |\langle \nu' | \nu'' \rangle|^2 \mathbf{P} \frac{1}{\epsilon_{\nu'} - \epsilon_{\nu''} - \xi} \quad (3.19)$$

and

$$\chi''(\xi) = \mu_{eg}^2 \pi \sum_{\nu'} |\langle \nu' | \nu'' \rangle|^2 \delta(\epsilon_{\nu'} - \epsilon_{\nu''} - \xi), \quad (3.20)$$

where **P** denotes the Cauchy principal part. We can relate the frequency-dependent susceptibility to the sine and cosine transforms of the population due to interference given by

$${\rm Re}[P_\phi^{\rm int}(\omega)] = \int_0^\infty dt \cos(\omega t) P_\phi^{\rm int}(t) \quad (3.21)$$

and

$${\rm Im}[P_\phi^{\rm int}(\omega)] = \int_0^\infty dt \sin(\omega t) P_\phi^{\rm int}(t). \quad (3.22)$$

Substitution of the general expression (3.13) in Eqs. (3.21) and (3.22) and combining results for in-phase and in-quadrature pulses to isolate the delta functions and the principal values yields

$${\rm Re}[P_0^{\rm int}(\omega)] \pm {\rm Im}[P_{\pi/2}^{\rm int}(\omega)] = 4\pi^2\mu_{eg}^2 \sum_{\nu'} |\langle \nu' | \nu'' \rangle|^2 \times |\mathscr{E}_1(\epsilon_{\nu'} - \epsilon_{\nu''})|^2 \delta(\epsilon_{\nu'} - \epsilon_{\nu''} - \Omega_L \mp \omega) \quad (3.23)$$

and

$${\rm Re}[P_{\pi/2}^{\rm int}(\omega)] \pm {\rm Im}[P_0^{\rm int}(\omega)] = 4\pi\mu_{eg}^2 \sum_{\nu'} |\langle \nu' | \nu'' \rangle|^2 \times |\mathscr{E}_1(\epsilon_{\nu'} - \epsilon_{\nu''})|^2 \mathbf{P} \frac{1}{\epsilon_{\nu'} - \epsilon_{\nu''} - \Omega_L \pm \omega}. \quad (3.24)$$

Because of the delta functions in Eq. (3.23), we can substitute $|\mathscr{E}_1(\Omega_L \pm \omega)|^2$ for $|\mathscr{E}_1(\epsilon_{v'} - \epsilon_{v''})|^2$, obtaining

$$\mathrm{Re}[P_0^{\mathrm{int}}(\omega)] \pm \mathrm{Im}[P_{\pi/2}^{\mathrm{int}}(\omega)] = 4\pi^2\mu_{eg}^2 \sum_{v'} |\langle v'|v''\rangle|^2 \times |\mathscr{E}_1(\Omega_L \pm \omega)|^2 \delta(\epsilon_{v'} - \epsilon_{v''} - \Omega_L \mp \omega). \quad (3.25)$$

We now recognize that the right-hand side of Eq. (3.25) is proportional to Eq. (3.20). The resulting expression for $\chi''(\Omega_L \pm \omega)$ is

$$\chi''(\Omega_L \pm \omega) = \frac{1}{4\pi^2|\mathscr{E}_1(\Omega_L \pm \omega)|^2} \times \{\mathrm{Re}[P_0^{\mathrm{int}}(\omega)] \pm \mathrm{Im}[P_{\pi/2}^{\mathrm{int}}(\omega)]\}. \quad (3.26)$$

Similarly, the right-hand side of Eq. (3.26) resembles $\chi'(\Omega_L \pm \omega)$, however, in this case the replacement of $|\mathscr{E}_1(\epsilon_{v'} - \epsilon_{v''})|^2$ with $|\mathscr{E}_1(\Omega_L \pm \omega)|^2$ is not exact. Nevertheless, division of Eq. (3.26) by the spectral intensity of the pulses yields

$$\frac{\mathrm{Re}[P_{\pi/2}^{\mathrm{int}}(\omega)] \mp \mathrm{Im}[P_0^{\mathrm{int}}(\omega)]}{4\pi|\mathscr{E}_1(\Omega_L \pm \omega)|^2} = 4\pi\mu_{eg}^2 \sum_{v'} |\langle v'|v''\rangle|^2 \frac{|\mathscr{E}_1(\epsilon_{v'} - \epsilon_{v''})|^2}{|\mathscr{E}_1(\Omega_L \pm \omega)|^2} \times \mathbf{P}\frac{1}{\epsilon_{v'} - \epsilon_{v''} - \Omega_L \pm \omega} \cong \chi'(\Omega_L \pm \omega). \quad (3.27)$$

Unless the pulses are arbitrarily short on a vibrational timescale so that $|\mathscr{E}_1(\epsilon_{v'} - \epsilon_{v''})|^2$ is uniform across the band, contributions to $\chi'(\Omega_L \pm \omega)$ from transitions more (less) distant from the peak of the pulse spectrum than $\Omega_L \pm \omega$ will be under (over) represented by the approximate identification (3.27).

Both the in-phase and in-quadrature results are required for the complete determination of the system's linear response. Expressions (3.26) and (3.27) can be easily generalized to include the rotational structure. In Sec. IV C we will compare the absorptive and dispersive parts of the linear susceptibility derived from experimental and calculated interferograms.

IV. RESULTS

A. Total fluorescence-detected interferograms: Rotational inhomogeneity

The experimental measurements of the interference contribution to the excited state population, as represented by the solid curves of Fig. 1, show several features that are characteristic of all of the time dependent in-phase interferograms. First, the magnitude of the signal at zero delay time is typically four to five times larger than the magnitude of the first recurrence feature. Second, the peaks, symmetrically disposed about $t_d = 0$, occur at intervals of delay that are inversely related to the vibrational level spacing of the (excited) B state of molecular iodine.[1] Third, in the case of phase-locking near wavelengths that correspond to prominent features in the absorption spectrum, the interferogram

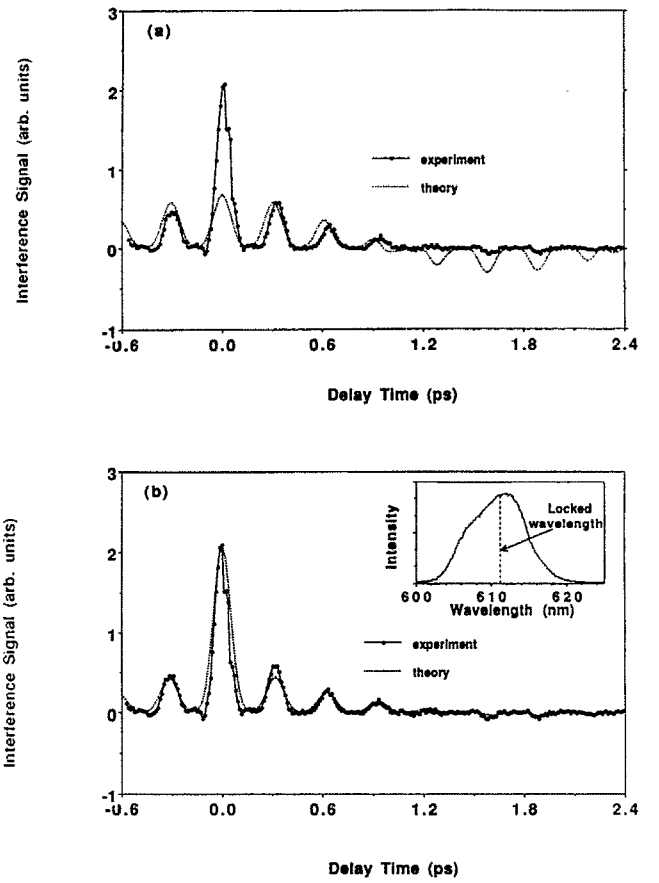

FIG. 1. (a) Comparison of an experimental in-phase interferogram locked at 611.43 nm with a calculated interferogram not including rotational degrees of freedom. Pulse parameters obtained with a Gaussian approximation to the experimental pulse intensity spectrum shown in inset of (b), are 611.6 nm carrier wavelength and 60.6 fs FWHM pulsewidth. (b) Same experimental interferogram as in (a) superimposed with a calculated interferogram that includes the rotational and vibrational degrees of freedom. The calculated interferogram assumes a 611.52 nm locked wavelength and a 60.6 fs FWHM pulswidth.

exhibits several positive features before crossing over to a region where the interference becomes negative going.

Figure 1(a) compares an experimental interferogram with a calculation of the interference contribution to the excited state population of molecular iodine which neglects the rotational degrees of freedom. The signals are normalized at the amplitude of the first recurrence feature. The two curves agree insofar as the theoretical curve predicts the experimentally observed crossover from constructive to destructive interference near 1.2 ps. However, the vibrations-only calculation is not in agreement with the relative amplitudes of the experimentally measured recurrence features.

Figure 1(b) shows the same experimental data superimposed with the theoretical interference contribution to the excited state population calculated according to Eqs. (3.10) and (3.11), which include both vibrational and rotational degrees of freedom. The Franck–Condon factors are taken from the work of Tellinghuisen,[31] the parameters for the

ground and excited states are taken from the work of LeRoy[32] and Barrow and Yee,[33] respectively, and the Gaussian pulse envelope is given by

$$E(t) = \exp(-t^2/2\tau^2); \quad \tau = \frac{\text{FWHM}}{2\,(\ln 2)^{1/2}}. \tag{4.1}$$

The experimental result and the calculation are normalized at $t_d = 0$. The pulse parameters used in this calculation are 60.6 fs FWHM pulse width, 611.6 nm carrier wavelength and 611.52 nm locked wavelength. Pulse width and carrier wavelength were determined from a Gaussian fit to the pulse intensity spectrum shown in the inset of Fig. 1(b). There is very good agreement between experimental and calculated interferograms.

The initial rapid decay of the interference signal, not seen in the vibrations-only calculation, results from the inhomogeneous distribution of transition frequencies due to the presence of many initial J'' values and the difference between the X-state and B-state rotational constants. For short enough delay times, we may neglect the rotational selection rules (i.e., $J' = J''$) and also the rotation–vibration interaction and centrifugal distortion contributions to the transition energies (all of which are included in our calculated interferograms). For a single pair of ground and excited vibronic states Eq. (3.11) becomes

$$P^{\text{int}}_{(v'',v')}(t_d) = \frac{1}{Z} e^{-\beta\epsilon_{v''}} |\mathscr{E}_1|^2 \frac{4\pi}{3} \mu_{eg}^2 |\langle v'|v''\rangle|^2 \times \sum_{J''} (2J''+1) e^{-\beta B'' J''(J''+1)} \times \cos[(\epsilon_{v',J'} - \epsilon_{v'',J''} - \Omega_L)t_d - \phi], \tag{4.2}$$

where it is further assumed that the pulse spectral intensity is constant in the range of rovibrational transition frequencies between the ground and the excited vibronic states. Converting the sum over J'' to an integral and integrating yields

$$P^{\text{int}}_{(v'',v')}(t_d) \cong \frac{1}{Z} e^{-\beta\epsilon_{v''}} |\mathscr{E}_1|^2 \frac{4\pi}{3} \mu_{eg}^2 |\langle v'|v''\rangle|^2 \times \frac{1}{(\beta B'')^2 + [(B'-B'')t_d]^2} \{\beta B'' \cos[(\epsilon_{v'} - \epsilon_{v''} - \Omega_L)t_d - \phi] - (B'-B'')t_d \sin[(\epsilon_{v'} - \epsilon_{v''} - \Omega_L)t_d - \phi]\}. \tag{4.3}$$

The ground and excited state rotational constants are $B'' = 0.037\ \text{cm}^{-1}$ and $B' = 0.029\ \text{cm}^{-1}$, respectively. The term proportional to the cosine dominates the interference signal at short delay times and has a Lorentzian envelope with a 0.74 ps decay constant. Expression (4.3) is expected to hold at short delay times as long as the pulse spectral intensity is uniform across the vibronic band. However, in Sec. IV B we will examine a case where the pulse shape has a considerable effect on the decay of the interference signal.

In this and all subsequent calculations it was found that shifting the theoretical locked wavelength 0.09 nm to the red of the experimental locked wavelength improved the agreement with the experiment. The small discrepancy is constant for all of the comparisons made here and for other data not shown, and is probably due to an inaccuracy in monochromator calibration.

B. Effect of pulse spectrum and lock wavelength on early time dynamics

Figure 2(a) compares the experimental and calculated interferograms obtained for an experimental locked wavelength of 607.06 nm. The calculated interferogram, assuming a Gaussian pulse shape with 50 fs FWHM pulsewidth, gives rather poor agreement at delay times less than 1.5 ps. The same experimental data as in Fig. 2(a) are compared in Fig. 2(b) with a calculated interferogram obtained using the experimental pulse intensity spectrum (see below). Figure 3 shows the in-phase interferogram for the locked wavelength of 611.36 nm together with a calculated interferogram obtained with the corresponding experimental intensity spectrum. Comparison of the power spectra of the experimental and theoretical interferograms (not shown) in Fig. 2(b) shows that the source of the disagreement between the two interferograms at short delay time is a much more pronounced 200 cm^{-1} feature in the calculated interferogram. We have not been able to account for this discrepancy.

The most striking difference between the interferograms in Figs. 2(b) and 3 is the behavior at short delay times. While the 607.06 nm locked interferogram [Fig. 2(b)] exhibits positive and negative interference signal, the 611.36 nm locked interferogram (Fig. 3) exhibits only positive interference until a time delay of over 1 ps. Such a difference cannot merely be attributed to the detuning of the locked wavelength from resonance with vibronic transitions. In fact, the 607.06 nm locked wavelength is closer to the $v' = 10 \leftarrow v'' = 2$ and $v' = 12 \leftarrow v'' = 3$ transitions than the 611.36 nm locked wavelength is to the $v' = 9 \leftarrow v'' = 2$ and $v' = 11 \leftarrow v'' = 3$ transitions, but the 607.06 nm locked interferogram exhibits destructive interference before one vibrational period. For a pulse spectrum uniform in the vicinity of the locked wavelength we would expect the 611.36 and 607.06 nm locked interferograms to be very similar, but in the present case the spectral shape of the pulses, different near the two locked components, plays an important role.

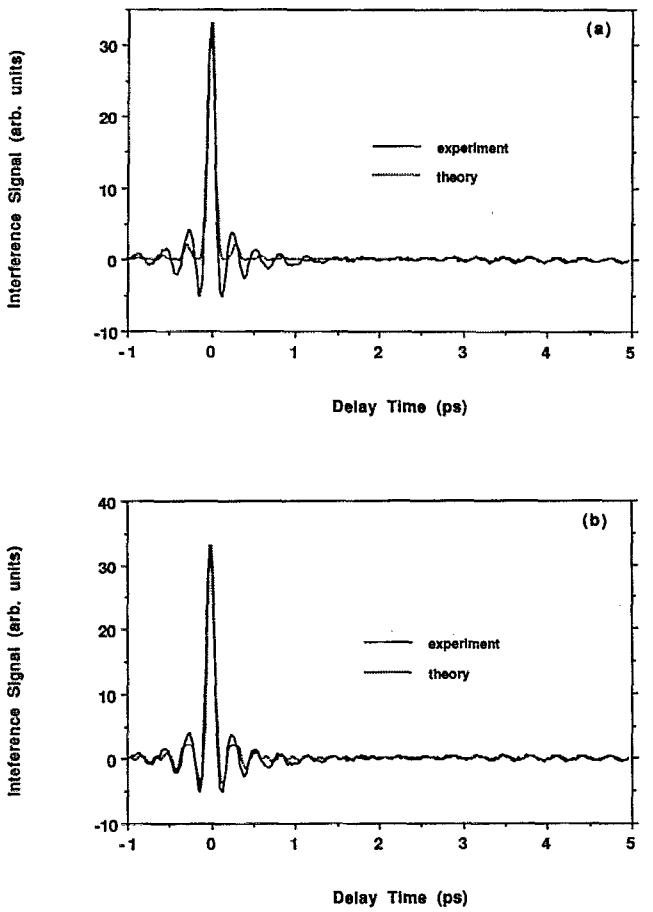

FIG. 2. (a) Experimental interferogram locked in phase at 607.06 nm superimposed with a calculated interferogram phase-locked at 607.15 nm with 609 nm carrier wavelength and 50 fs FWHM pulsewidth Gaussian pulse. (b) Same experimental interferogram as in (a) compared to a calculated interferogram locked in phase at 607.15 nm using the experimental pulse intensity spectrum.

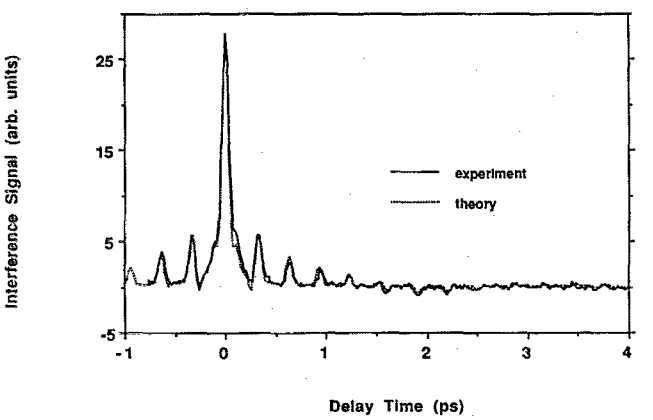

FIG. 3. Experimental interferogram locked in phase at 611.36 nm compared to a calculated interferogram with 611.45 nm locked wavelength using the experimental pulse intensity spectrum.

In order to understand the origin of the observed difference between the 607.06 and 611.36 nm locked interferograms, we will focus on the vibronic transitions that are closest to the locked wavelength, namely, the $\nu' = 10 \leftarrow \nu'' = 2$ transition for locking at 607.06 nm and the $\nu' = 9 \leftarrow \nu'' = 2$ transition for locking at 611.36 nm. The ground state vibrational levels $\nu'' = 2$ and $\nu'' = 3$ are the largest contributors to the interference signal due to sizable thermal population and good Franck–Condon overlap. The $\nu'' = 0$ and $\nu'' = 1$ states, although much more populous, have small Franck–Condon overlap with electronically excited vibrational states in the spectral region spanned by the laser pulses. The states with $\nu'' > 3$ have too small a thermal population to contribute significantly. We will only consider the interference signal originating in $\nu'' = 2$ since the $\nu'' = 3$ contribution is similar at short delay times as a result of the $\sim$2:1 ratio in vibrational frequencies in the X state and the B state.

Figures 4(a) and 4(b) show the pulse spectra for the 607.06 and 611.36 nm locked interferograms, respectively. The solid line indicates the locked wavelength, nearly coincident with the bare vibronic transition in each case. Almost

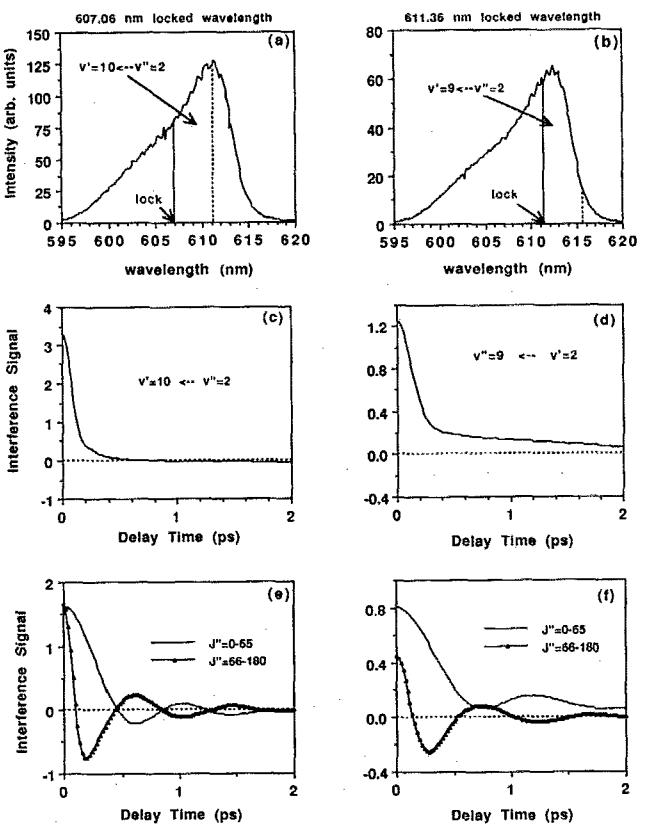

FIG. 4. (a) and (b) Pulse spectral profiles for locking at 607.16 and 611.36 nm, respectively. Regions bordered by the solid and dashed lines are responsible for driving the indicated transitions. (c) and (d) Calculated interference signal due to the $\nu' = 10 \leftarrow \nu'' = 2$ transition for locking at 607.15 nm and the $\nu' = 9 \leftarrow \nu'' = 2$ transition for locking at 611.45 nm, respectively. (e) and (f) Calculated interference signal shown in (c) and (d), respectively, split into the $J'' = 0$–65 and $J'' = 66$–180 contributions.

all rovibronic transition energies lie to the red of the bare vibronic transition energy because the bandhead comes very early ($J'' = 8$). Therefore, the region of the pulse spectrum bordered by the solid line (the locked wavelength) and the dashed line is responsible for driving the rovibronic transitions between the vibronic states indicated. Figures 4(c) and 4(d) show the calculated interference signal resulting from all of the rovibronic transitions driven by the portions of the pulse spectra enclosed by the solid and dashed vertical lines. Figures 4(e) and 4(f) show the separate contributions of the $J'' = 0$–65 and $J'' = 66$–180 rovibronic transitions to the total interference signal. For the case of the 607.06 nm locked wavelength, the two components shown in Fig. 4(e) are of approximately equal magnitude, since the spectral shape of the pulse in the outlined region in Fig. 3(a) is not changing rapidly. The two components combine to yield a near-zero interference signal. For the case of 611.36 nm experimental phase locking, however, the two components shown in Fig. 4(f) are quite different in magnitude since the $J'' = 66$–180 component sees a much less intense pulse spectrum than is seen by the $J'' = 0$–65 component. This results in the overall positive interference signal shown in Fig. 4(d). Also, the initial decay in Fig. 4(d) is slower than in Fig. 4(c) because the pulse spectrum reduces the effective extent of the rotational inhomogeneity in Fig. 4(d).

Calculations of the interference signal arising from all vibronic transitions other than the one closest to the locked wavelength (not shown) have positive and negative interference features at short delay times. This is true for both locked wavelengths. Thus in the case of 607.06 nm experimental locked wavelength, the contribution of the transition closest to resonance does not affect the short time delay interference signal after the initial decay. In the case of 611.36 nm experimental locked wavelength, however, the transition closest to resonance with the locked wavelength contributes positive interference signal, resulting in the overall positive interferogram at short delay times.

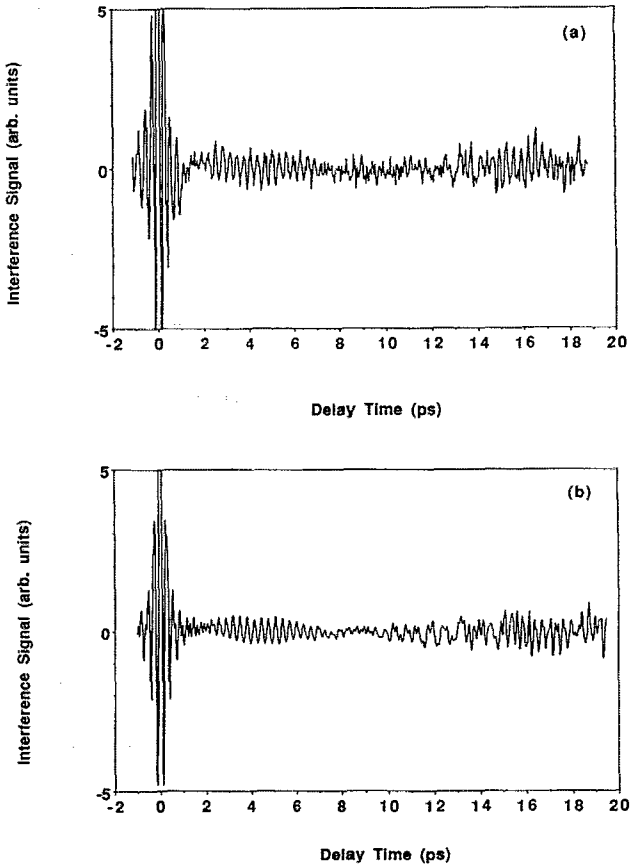

FIG. 5. (a) Experimental interferogram taken with in-phase pulses locked at 607.06 nm for time delays up to 19 ps. The $t_d = 0$ feature has been cut off. (b) Calculated interferogram phase-locked at 607.15 nm.

C. Long delay time interferogram

It is of interest to understand the wave packet evolution at long delay times. It has been shown by Zewail and coworkers that rovibrational wave packets recur for long periods of time.[6] This is a reflection of uninterrupted evolution of the relative phase factors of the individual excited state rovibrational levels. We are able to monitor the evolution of the wave packet with sensitivity to both the relative quantum phases among the individual excited rovibrational levels and the relative phase between each contributing excited rovibrational state and the initial ground state level. Figure 5(a) shows the experimental interferogram over 19 ps delay and Fig. 5(b) the corresponding theoretical result. It may be seen that both Figs. 5(a) and 5(b) show a diminished peak amplitude at about 9 ps delay and a reestablishment of a regular peak pattern from 14 to 19 ps delay. The period of the 2–8 and 14–19 ps recurrences is approximately 300 fs. The region in Fig. 5(a) between 9 and 14 ps delay shows a nonzero interference amplitude but does not yield any obvious periodicity.

It is helpful to examine the time scale on which different molecular parameters affect the interferogram. As explained earlier, the initial rapid decay of the interference signal can be attributed to the range of transition energies resulting from the thermal distribution of initial rotational states ("inhomogeneous" dephasing). The ~5 ps "wobble" seen in the experimental and calculated interferograms shown in Fig. 5 is a result of the vibrational inhomogeneity caused by the anharmonicity of the B state. Figure 6 shows the separate contributions to the interferogram from the $v'' = 2$ and $v'' = 3$ initial vibronic states that contribute to the observed interferograms locked near 607 nm. The contribution from $v'' = 2$ has more frequent extrema in part because the wave packet originating in $v'' = 2$ vibronic state evolves in a lower region (v' near 10) of the B state than does the wave packet originating in the $v'' = 3$ vibronic state (v' near 12).

The rotational dynamics, arising from the superposition of the $J' = J'' \pm 1$ levels, do not play a significant role in the appearance of the calculated interferogram until time delays of over 7 ps. The energy splitting between the $J'' + 1$ and $J'' - 1$ levels is $B'(4J'' + 2)$, corresponding to 4.4 ps for $J'' = 65$. Thus the inhomogeneous dephasing and the lack of

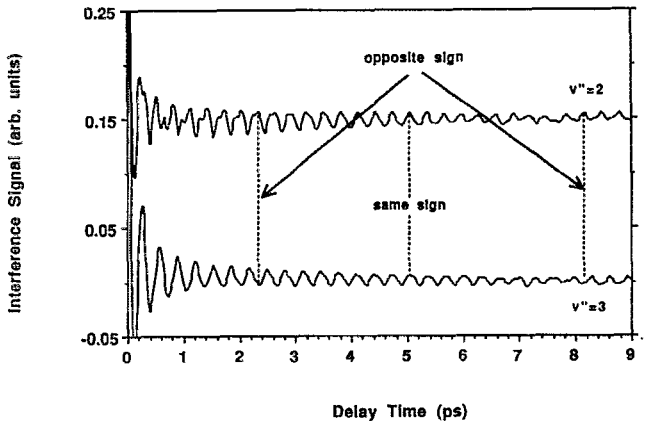

FIG. 6. Contributions from $v'' = 3$ and $v'' = 2$ (shifted vertically) to the interferogram shown in Fig. 5(b).

a single time scale for rotational dynamics, both due to the initial thermal distribution of rotational levels, makes it difficult to discern the effects of rotational dynamics. The absence of sensitivity to spatial rotational dynamics, while not inherent to the technique, is in contrast with the techniques of rotational coherence spectroscopy.[34]

Our calculations include the nuclear spin degeneracy factors of 5/6 and 7/6 for even and odd J'', respectively. The inclusion of spin statistics affects the interferogram beyond about 7 ps. This corresponds to the onset of sensitivity to the discrete nature of the inhomogeneous J'' distribution.

The rotation–vibration interaction introduces energy shifts of the order of 0.5 cm^{-1} and, therefore, affects the interferogram at time delays greater than 15 ps. Centrifugal distortion is of magnitude of 0.1 cm^{-1} and would be expected to affect the interferogram at time delays on the order of 80 ps.

The J dependence of the Franck–Condon factors does not play a role in the appearance of the interferogram. Comparison of interferograms calculated with $J = 0$ Franck–Condon factors and J-dependent Franck–Condon factors showed negligible differences. The Franck–Condon factors in the region spanned by the pulses differ by 5%–10% for $J = 0$ and $J = 100$.[31] Throughout our calculations we have made an assumption that the electronic transition dipole moment is constant; it varies by less than 5% in the region of thermally occupied vibrational states. Interferograms calculated with an electronic dipole moment that is linearly dependent on the R centroid[35] were found to be virtually identical to those shown here.

Finally, the contributions of other electronic states in the region of the B state are not included in our analysis. The two other bright states in the region, the A state and the B'' state, are repulsive in the frequency range of these experiments.[31] The effect of these states on the fluorescence interferogram is only of possible importance at very short time delays (< 100 fs).

D. In-quadrature phase-locking and the frequency-dependent susceptibility

As discussed in the theoretical section, the two-pulse phase-locked measurements monitor the evolution of the linear polarization induced in the molecule by the first pulse. The in-phase measurements compare the phase evolution to a zero degree reference. It is also possible to lock the phases of the two pulses in quadrature, corresponding to comparison with a 90 deg reference. Figure 7 shows the interferogram produced at a locked wavelength of 607.06 nm with in-quadrature phase-locked pulse pairs. The signal in Fig. 7 was recorded under identical conditions as the in-phase signal in Fig. 2(b). The two-pulse delays at each recorded time point differ by 1/4 optical period between the in-phase and in-quadrature interferograms, or about 0.4 fs.

Figure 8(a) shows the absorptive and dispersive parts of the frequency-dependent linear susceptibility calculated from the in-phase and in-quadrature interferograms (see Sec. III B). The absorptive part represents the dissipation of energy from the laser pulses, and the dispersive part represents the resonant contribution to the index of refraction. The absorptive part in Fig. 8(a) is in agreement with the rotationally unresolved absorption spectrum of molecular iodine.[36] Figure 8(b) shows the absorptive and dispersive parts of $\chi(\Omega_L \pm \omega)$ obtained from calculated in-phase and in-quadrature interferograms locked at 607.15 nm using the experimental intensity spectrum. The peak widths in the experimentally and theoretically derived absorption and dispersion spectra correspond to the inverse of the maximum delay time rather than the intrinsic line widths, since the radiative lifetime of the B-state rovibronic levels is on the order of several microseconds and greatly exceeds the maximum inter-pulse delay. The agreement between experiment and theory is good overall. The discrepancy in the magnitude of the 200 cm^{-1} peaks in the absorptive and dispersive parts of the susceptibility between Figs. 8(a) and 8(b) is due to the previously mentioned disagreement between the experimental and theoretical interferograms (see Sec. IV B).

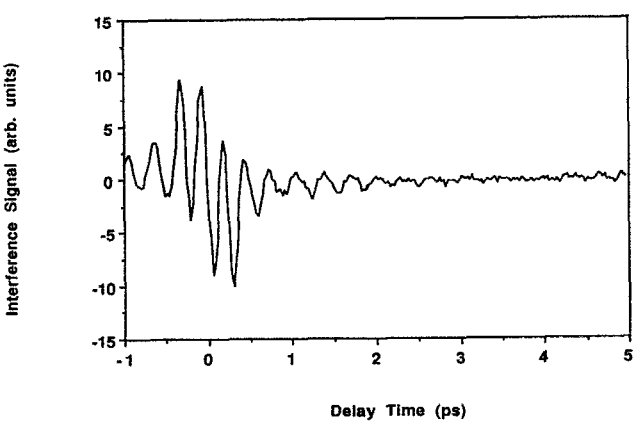

FIG. 7. In-quadrature experimental interferogram phase-locked at 607.06 nm.

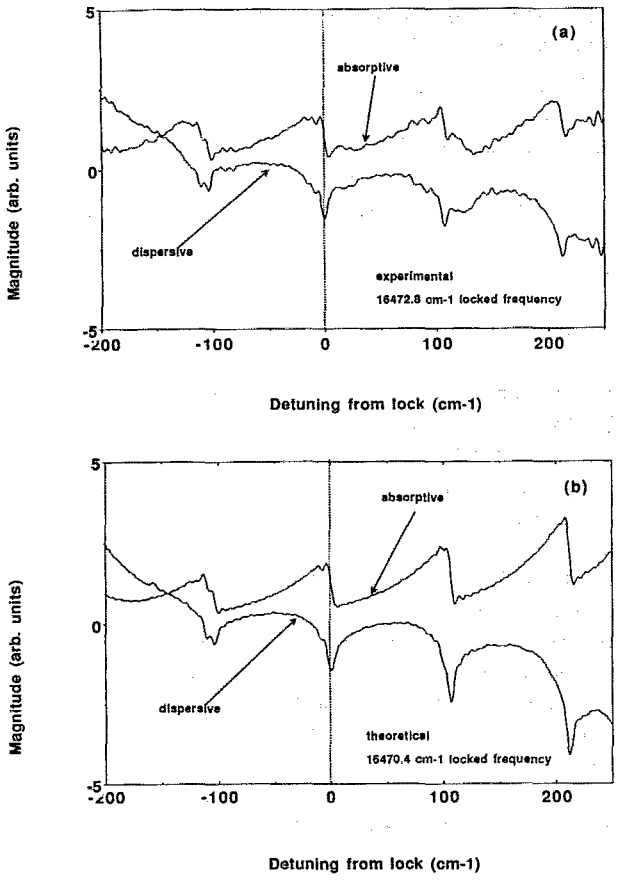

FIG. 8. (a) Absorptive and dispersive parts of the linear susceptibility calculated from the experimental in-phase and in-quadrature interferograms shown in Figs. 2(b) and 7, respectively. (b) Absorptive and dispersive parts of the linear susceptibility calculated from theoretical interferograms corresponding to experimental interferograms shown in Figs. 7 and 2(b), respectively.

E. Spectrally resolved emission detection

The previous experimental and theoretical results have dealt with the interference contribution to the excited state population as measured by detecting the integrated total fluorescence. This section will focus on the two-pulse phase-locked interferograms observed for spectrally selected $B \rightarrow X$ fluorescence bandpasses at several different wavelengths. The observed and calculated interferograms reflect the dynamics of emission wavelength selected portions of the excited state wave packet.

Our calculations of dispersed emission interferograms use the golden rule. They consist of two parts: determination of the population due to interference in each of the rovibrational levels of the electronic excited state and the determination of spontaneous emission from each one of these states through a given spectral window. The interaction of the molecule with the pulses is treated using the experimentally determined spectral shape of the amplified laser pulses. As discussed above, the two-field dependent integrated fluorescence is directly proportional to the interference contribution to population in the B state. The calculation of emission through a spectral window requires more information about the X state of iodine than provided in the work of Tellinghuisen.[31] Reference 31 includes only the Franck–Condon factors for $v'' = 0$–5, which are insufficient for the determination of emission from the B state. If we consider emission from the B state explicitly, we must include all the transitions that fall within the chosen spectral window. We use Morse oscillator wave functions to calculate the Franck–Condon factors not provided in Ref. 31. The spectral window used in our calculations is triangular corresponding to the slit function of the monochromator used in the experiment.

A 2.5 nm spectral window (FWHM, triangular) centered at some emission wavelength is a common feature for the results shown in Fig. 9. The incident locked wavelength of 607.06 nm is coincident with the $v'' = 2 \rightarrow v' = 10$ and $v'' = 3 \rightarrow v' = 12$ transitions. Figure 9(a) has the 2.5 nm spectral detection window centered at 598.0 nm for the ex-

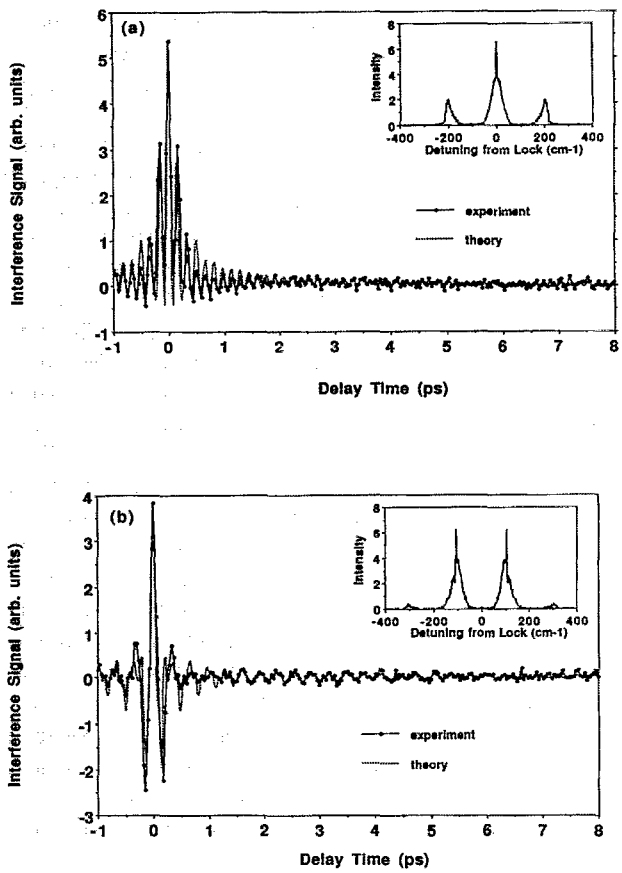

FIG. 9. (a) Experimental interferogram obtained with spectrally resolved fluorescence detection with the spectral window centered at 598.0 nm superimposed with a calculated interferogram with spectral window centered at 598.5 nm. The power spectrum of the experimental interferogram is shown in the inset. The in-phase locked wavelength is 607.06 nm. (b) Same as Fig. 8(a) except the experimental and theoretical detection windows are at 594.0 and 594.5 nm, respectively.

perimental interferogram and at 598.5 nm for the calculated interferogram. The associated power spectrum is shown in the inset. The spectral window is positioned to detect the wavelength corresponding to the $v' = 10 \rightarrow v'' = 1$, $v' = 12 \rightarrow v'' = 2$, and $v' = 14 \rightarrow v'' = 3$ transitions. Depending on the initial ground vibrational state, the interference population in $v' = 10$, 12, and 14 oscillates at 0 or ~ 200 cm^{-1}, since the excited vibronic states detected are either at the locked wavelength or detuned by 2 excited state vibrational quanta.

The interferogram of Fig. 9(b) was obtained for a spectral window centered at 594.0 nm for the experimental interferogram and at 594.5 nm in the calculation. The spectral window is coincident with $v' = 11 \rightarrow v'' = 1$, $v' = 13 \rightarrow v'' = 2$ and $v' = 15 \rightarrow v'' = 3$ transitions. The associated power spectrum is shown in the inset. This time the spectral window is positioned to detect the wavelength corresponding to the $v' = 11 \rightarrow v'' = 1$, $v' = 13 \rightarrow v'' = 2$, and $v' = 15 \rightarrow v'' = 3$ transitions. The interference population in each of the detected excited vibronic states oscillates at ~ 100 or ~ 300 cm^{-1}, giving rise to the corresponding features in the observed interferogram and the power spectrum.

The 4 nm separation of the spectral windows of Fig. 9, corresponding to 110 cm^{-1}, is approximately equal to the excited state vibrational level spacing and approximately half of the 210 cm^{-1} ground state vibrational level spacing, therefore enabling the detection of the interference population in different subsets of excited state vibrational levels.

The dispersed fluorescence calculations are in good agreement with experiments, but some differences remain, particularly at time delays less than 1 ps. Some of the discrepancies can be attributed to the low point density in the experimental data. Also, the precise location of the spectral window is known only to within $\pm$ 0.5 nm. The agreement is better at negative delay times although the interference signal is ideally symmetric about zero delay.

F. Dependence of the interferogram on the spectral window width

It is also important to consider the effect of the width of the spectral window on the form of the fluorescence detected interferogram. Three experimental interferograms for 10, 2.5, and 0.5 nm FWHM spectral windows are shown in Figs. 10(a), 10(b), and 10(c), respectively. Each figure also shows the calculated spectrally windowed interferograms. In all three cases the spectral window is centered at 616 nm[37] while the locked wavelength is maintained at 607.06 nm. As the detection window is narrowed, the observed interferogram decays more slowly. The associated power spectra, without deconvolution for the spectral density of the two-pulse response function, are shown in the insets. The three interferograms become progressively more simply cosinusoidal as compared to Fig. 2. Even though the 10 nm detection window is comparable to the width of the pulse spectrum the long Franck–Condon progressions in emission yield a range of emission wavelengths much broader than simply the pulse spectral width.

Narrowing the spectral detection window, in this case, acts to filter out frequency components at 110 cm^{-1}, due to the interference population in $v' = 9$, 11, and 13. The interferogram with a 0.5 nm window, the narrowest detection window used here, most closely resembles a purely cosinu-

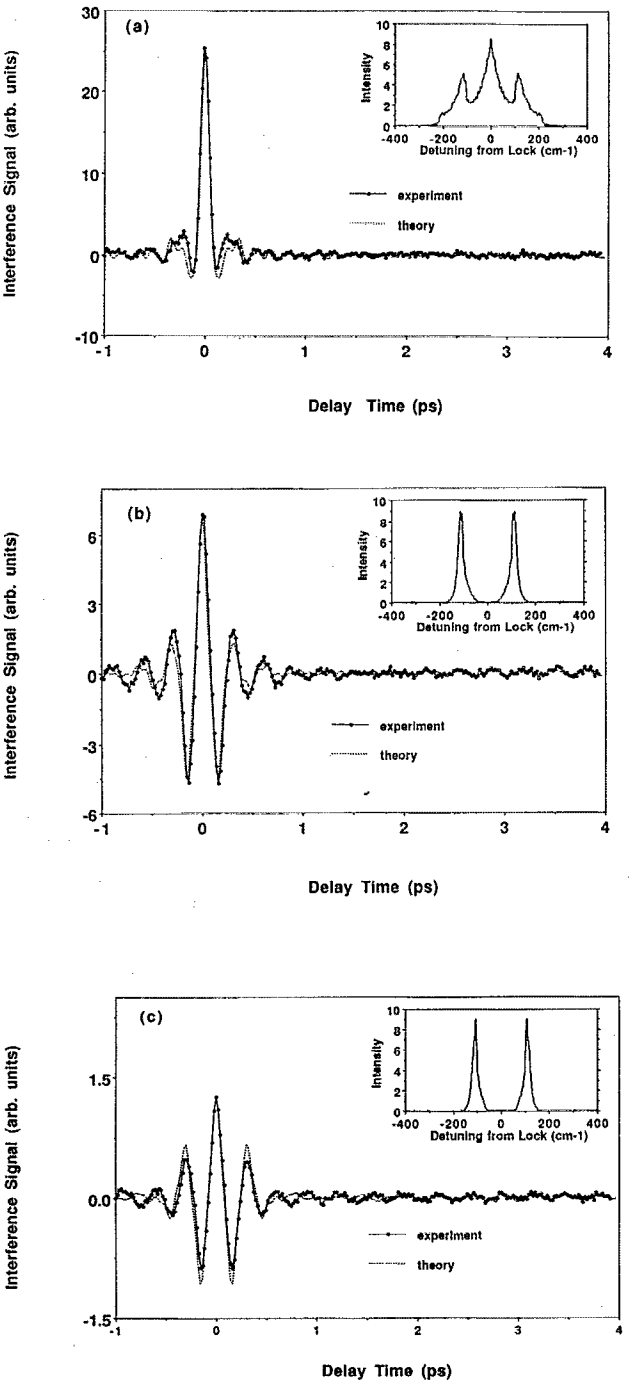

FIG. 10. (a) Experimental interferogram obtained with spectrally resolved fluorescence detection with a 20 nm spectral window centered at 616 nm superimposed with a calculated interferogram with the spectral window centered at 618.5 nm (Ref. 37). The power spectrum of the experimental interferogram is shown in the inset. The composite exciting pulse pair is locked in phase at 607.06 nm. (b) and (c) Same as (a) except that the spectral window is narrowed to 5 and 1 nm, respectively.

soidal signal. Such a temporal form reflects a reduction in the distribution of both vibrational and rotational states that are detected.

V. DISCUSSION AND CONCLUSION

As mentioned in Sec. I, Bavli, Engel, and Metiu[23] have recently performed calculations, properly including the rovibronic structure of I_2, which agree with the finding that thermal occupation of many ground state J levels and the electronic state dependence of the rotation constant account for the observed decay of the interferogram. Other recent calculations[38] have investigated the consequences of imposing a relatively simple phase chirp to one pulse of a phase-locked pair. Among other results, we have identified the piecewise linear phase structure necessary to compensate the effects of rotational inhomogeneous dephasing. The significance of this result is to allow the superposition of two vibrational wave packets with the same relative phase regardless of J''. Such a capability could be of use in preparing prescribed excited state wave forms for purposes of controlling molecular dynamics.[16]

The fundamental significance of phase-locked pulse pair measurements is understood upon realizing that the two-pulse interference experiment (combining in-phase and in-quadrature data) is a direct time domain measurement of the autocorrelation function of the dipole moment operator of the absorbing molecules. When the molecules do not interact on the time scale of the experiment, the correlation function determines the absorption spectrum.

Spectroscopy with pairs of phase-locked pulses enables the direct determination of the evolution of the polarization induced by the initial laser pulse and described by the complex time-dependent linear susceptibility, $\chi(t)$. By Fourier transformation of the experimentally determined $P_0^{\rm int}(t_d)$ and $P_{\pi/2}^{\rm int}(t_d)$ both the absorptive and the dispersive parts of the frequency-dependent linear susceptibility, $\chi(\omega)$, are obtained directly. In the limit of infinite duration pulse excitation and for on-resonance excitation such measurements would yield the absorption coefficient at a single frequency but would not give information about the real part of $\chi(\omega)$. Application of δ-function pulses would allow the determination of the complete frequency dependence of complex $\chi(\omega)$ from the in-phase and in-quadrature measurements regardless of the locked wavelength.

The derivation presented in Sec. III is appropriate for the case where phase relaxation of the optically prepared superposition state is long compared to the time delay between two pulses. This situation is well approximated in the present room temperature gas phase experiments where the mean time between phase interrupting collisions is of the order 100 ns (Ref. 39). A more general formulation that is appropriate for dense gas or condensed phase environments would have to include population and phase relaxation. Interestingly, the experimental approach to determining the complex susceptibility from the measured in-phase and in-quadrature interferograms remains appropriate unless the excited state is depopulated too rapidly to measure the population by spontaneous emission.

There is an interesting connection between wave packet interferometry with arbitrarily abrupt, phase controlled pulses, and the wave packet picture of continuous wave linear response developed by Heller[19,29] and others.[20-22,40] Heller's wave packet picture comes from writing the frequency dependent susceptibility [(3.18) and (3.15b)] in the form

$$\chi(\xi) = i\mu_{eg}^2 \int_0^\infty dt \, \langle v'' | \exp[\, i(\xi - H_e + \epsilon_{v''})t \,] | v'' \rangle, \tag{5.1}$$

in which the key quantity is the overlap function

$$\langle v'' | \exp[\, -iH_e t \,] | v'' \rangle \equiv \langle v'' | v''(t) \rangle \tag{5.2}$$

of the ground state wave function propagated under the excited state nuclear Hamiltonian.

In the limit of pulses arbitrarily short on a vibrational time scale, the in-phase and in-quadrature interference signals (3.14) can be combined to yield the overlap function (5.2) with the optical frequency oscillations removed

$$\frac{1}{4\pi |\mathscr{E}_1|^2 \mu_{eg}^2} [\, P_0^{\rm int}(t) - iP_{\pi/2}^{\rm int}(t) \,] = \exp[\, i(\Omega_L + \epsilon_{v''})t \,] \langle v'' | v''(t) \rangle. \tag{5.3}$$

Substituting Eq. (5.3) into Eq. (5.1) we obtain

$$\chi''(\Omega_L \pm \omega) = \frac{i}{4\pi |\mathscr{E}_1|^2} \int_0^\infty dt \exp[\, \pm i\omega t \,] \times [\, P_0^{\rm int}(t) - iP_{\pi/2}^{\rm int}(t) \,], \tag{5.4}$$

which is equivalent to the expression obtained from Eqs. (3.16) and (3.18). The experimentally determined quantity (5.3) is an optically demodulated version of the overlap kernel studied by Heller and co-workers. In this connection, it is worth pointing out that the in-phase and in-quadrature interferograms for a multimode system exhibiting nonadiabatic dynamics have recently been calculated by Coalson, determining the continuous wave spectrum for such a system (see Figs. 1 and 2 of Ref. 20).

APPENDIX A: DERIVATION OF THE FLUORESCENCE INTERFEROGRAM SIGNAL BY A DENSITY MATRIX DESCRIPTION OF LINEAR RESPONSE THEORY

The fluorescence detected interference contribution to the excited state population due to a pair of resonant phase-locked pulses can also be derived via the well-known formalism of the density matrix description of optical spectroscopies. One advantage of this approach is that damping due to both intramolecular and solvent interactions can be properly incorporated. Furthermore, this theoretical framework allows this phase-locking technique to be formally pictured as a pump–probe spectroscopy and allows these experiments to be more readily contrasted with other recent ultrafast pump–probe studies.

The contribution of the $g \rightarrow e$ molecular transition to the linear polarization at time t resulting from the perturbation of an applied radiation field at time t' is given by

$$P^1(t) = \sum_e [\, \mu_{eg}^* \rho_{eg}^1(t) + \text{c.c.} \,], \tag{A1}$$

where

$$\rho^1_{eg}(t) = i/\hbar \int_0^\infty dt'\, \mu_{eg}\, \mathscr{E}_1(t-t') \times \exp[-(i\omega_{eg} + 1/T_2)t']\rho^0_{gg} \tag{A2}$$

and

$$\mathscr{E}_1(t) = \tfrac{1}{2}E_0 \exp(-t^2/2\tau^2)\,[\exp(i\Omega t) + \exp(-i\Omega t)]. \tag{A3}$$

The linear response function employed above is the usual optical Bloch equation solution form. μ_{ge} is the transition moment of the $g \rightarrow e$ excitation, ρ^0_{gg} is the equilibrium population of initial state g and $\omega_{eg} = (\epsilon_e - \epsilon_g)/\hbar$. The optical coherence created by one field of the first pulse of the phase-locked pulse pair decays with a rate given by the optical or electronic dephasing time $1/T_2$. When the pulse duration is shorter than the optical dephasing time, the resulting linear polarization in the rotating wave approximation is

$$P^1(t) = i(\pi/2)^{1/2}\frac{\tau}{\hbar}E_0 \sum_e |\mu_{eg}|^2 \times \exp[-i(i\omega_{eg} + 1/T_2)t] \times \exp[-(\omega_{eg} - \Omega)^2\tau^2/2] + \text{c.c.} \tag{A4}$$

The mean energy loss/gain of the material due to the interaction of this linear polarization with a time delayed phase-locked field $\mathscr{E}_2(t)$ is given by[41]

$$W(t_d) = -\int_{-\infty}^{\infty} P^1(t)\frac{\partial}{\partial t}\mathscr{E}_2(t)dt = \frac{iE_0\Omega}{2}\left\{\sum_e \int_{-\infty}^{\infty} dt\, \mu_{eg}\rho^1_{eg}(t)^* \times \exp[-(t-t_d)^2/2\tau^2 \times \exp[i(\Omega t + (\Omega_L - \Omega)t_d + \phi)] - \text{c.c.}\right\}, \tag{A5}$$

where

$$\mathscr{E}_2(t) = \tfrac{1}{2}E_0 \exp[-(t-t_d)^2/2\tau^2] \times [\exp[i(\Omega t + (\Omega_L - \Omega)t_d + \phi)] + \text{c.c.}]. \tag{A6}$$

A positive value of $W(t_d)$ corresponds to loss in optical power of the transmitted probe beam, i.e., net positive work has been done by the fields on the material system. Thus the cycle averaged work done per pulse pair (dimensions of energy) due to the interaction of the probe field delayed by time t_d from the driving "pump" field when the electronic dephasing time is again taken to be longer than the pulse duration is given by

$$W(t_d,\phi) = \frac{\pi\tau^2 E_0^2\Omega}{\hbar}\rho^0_{gg}\exp(-t_d/T_2) \times \sum_e |\mu_{eg}|^2 \exp-(\omega_{eg} - \Omega)^2\tau^2 \times \cos[(\Omega_L - \omega_{eg})t_d + \phi]. \tag{A7}$$

The functional form of this result is identical to the expression derived above [Eqs. (3.10) and (3.11)] and in paper I [Eq. (4.42)] for the two-pulse interference contribution to the excited state population derived by first-order perturbation theory, except for the appearance of damping. The effect of this dephasing term, however, is not detectable for the I_2 gas phase experiments described here due to the long lifetime of the B-state levels ($t_d/T_2 \sim 10^{-4}$). The two-field interference contribution to the excited state population [Eqs. (3.10) and (3.11)] is exactly recovered when the work expression above [Eq. (A7)] is divided by the absorption quantum $\hbar\Omega$ and molecular states are taken to be rovibronic levels, $|g\rangle = |gv''J''\rangle$ and $|e\rangle = |ev'J'\rangle$.

It should also be noted that the absorption contribution due to these phase-locked fields can be calculated by the other physically equivalent pulse sequence description shown below

$$W(t_d,\phi) = -\int_{-\infty}^{\infty} P^1(t+t_d)\frac{\partial}{\partial t}\mathscr{E}_1(t)dt. \tag{A8}$$

Acknowledging the finite bandwidth of the resonant phase-locked transitions, the in-phase and in-quadrature interferograms calculated according to Eq. (A7) above can be combined to yield expressions analogous to Eqs. (3.23) and (3.24)

$$\begin{aligned}
&\mathrm{Re}[W(\omega,0) \pm \mathrm{Im}[W(w,\pi/2)] \\
&= \frac{\pi\Omega}{\hbar}|\mu_{eg}|^2 \sum_{v'} |\langle v'|v''\rangle|^2 |\mathscr{E}_1(\epsilon_{v'} - \epsilon_{v''})|^2 \\
&\quad \times \frac{1/T_2}{(\epsilon_{v'} - \epsilon_{v''} - \Omega_L \pm \omega)^2 + (1/T_2)^2}, \\
&\mathrm{Re}[W(\omega,\pi/2) \mp \mathrm{Im}[W(w,0)] \\
&= \frac{\pi\Omega}{\hbar}|\mu_{eg}|^2 \sum_{v'} |\langle v'|v''\rangle|^2 |\mathscr{E}_1(\epsilon_{v'} - \epsilon_{v''})|^2 \\
&\quad \times \frac{-(\epsilon_{v'} - \epsilon_{v''} - \Omega_L \pm \omega)}{(\epsilon_{v'} - \epsilon_{v''} - \Omega_L \pm \omega)^2 + (1/T_2)^2},
\end{aligned} \tag{A9}$$

where

$$W(\omega,\phi) = \int_0^\infty \exp(i\omega t_d)\, W(t_d,\phi)dt_d. \tag{A10}$$

The corresponding linear susceptibility components are given by

$$\chi'(\Omega_L \pm \omega) = \frac{|\mu_{eg}|^2}{\hbar}\sum_{v'} |\langle v'|v''\rangle|^2 \times \frac{(\epsilon_{v'} - \epsilon_{v''} - \Omega_L \pm \omega)}{(\epsilon_{v'} - \epsilon_{v''} - \Omega_L \pm \omega)^2 + (1/T_2)^2}$$

and

$$\chi''(\Omega_L \pm \omega) = \frac{|\mu_{eg}|^2}{\hbar}\sum_{v'} |\langle v'|v''\rangle|^2 \times \frac{1/T_2}{(\epsilon_{v'} - \epsilon_{v''} - \Omega_L \pm \omega)^2 + (1/T_2)^2}. \tag{A11}$$

Thus formally for dissipative systems, the real and imaginary parts of the linear susceptibility can only be determined from the in-phase and in-quadrature fluorescence interferograms for temporal delta function pulses [$|\mathscr{E}_1(\epsilon_{v'} - \epsilon_{v''})|^2 = (2\pi)^{-1}$]. However, as discussed in

Sec. III, when the absorption line shape is taken to be a delta function, the corresponding real and imaginary components of $\chi'(\Omega_L \pm \omega)$ can also be determined from the experimentally observed interferograms. This approximation will be quite good when the experimental delay time is much shorter than the optical dephasing time. This condition is easily satisfied for the experiments described here $(t_d/T_2 \sim 10^{-4})$.

ACKNOWLEDGMENTS

The research reported in this paper was supported by grants from the National Science Foundation. Acknowledgment is made to the donors of the Petroleum Research Fund, administered by the American Chemical Society, for partial support of this research. We thank Dr. Seung-Eun Choi for early numerical work contributing to the rotational calculations presented here. Helpful conversations with Warren S. Warren, Horia Metiu, and Ranaan Bavli are gratefully acknowledged. N. F. S. acknowledges the NSF for a postdoctoral fellowship.

We dedicate this paper to Roger Carlson.

[1] N. F. Scherer, R. J. Carlson, A. Matro, M. Du, A. J. Ruggiero, V. Romero-Rochin, J. A. Cina, G. R. Fleming, and S. A. Rice, J. Chem. Phys. **95**, 1487 (1991); N. F. Scherer, A. J. Ruggiero, M. Du, and G. R. Fleming, *ibid.* **93**, 856 (1990).

[2] A. M. Weiner, J. P. Heritage, and R. N. Thurston, Opt. Lett. **11**, 153 (1986); R. N. Thurston, J. P. Heritage, A. M. Weiner, and W. J. Tomlinson, IEEE J. Quantum Electron. **QE-22**, 682 (1986); A. M. Weiner and J. P. Heritage, Rev. Phys. Appl. **22**, 1619 (1987); A. M. Weiner, D. E. Leaird, G. P. Wiederecht, and K. A. Nelson, Science **247**, 1317 (1990).

[3] F. Spano, M. Haner, and W. S. Warren, Chem. Phys. Lett. **135**, 97 (1987); *Ultrafast Phenomena V*, edited by G. R. Fleming and A. Siegman (Springer, Berlin, 1986), p. 514; W. S. Warren and M. S. Silver, Adv. Mag. Reson. **12**, 247 (1988).

[4] M. J. Rosker, F. W. Wise, and C. L. Tang, Phys. Rev. Lett. **57**, 321 (1986); I. A. Walmsley, F. W. Wise, and C. L. Tang, Chem. Phys. Lett. **154**, 315 (1989); I. A. Walmsley, M. Mitsunaga, and C. L. Tang, Phys. Rev. A **38**, 3566 (1988).

[5] J. Chesnoy and A. Mokhtari, Phys. Rev. A **38**, 3566 (1988).

[6] R. M. Bowman, M. Dantus, and A. H. Zewail, Chem. Phys. Lett. **161**, 297 (1989); M. Grubele, G. Roberts, M. Dantus, R. M. Bowman, and A. H. Zewail, *ibid.* **166**, 459 (1990); J. J. Gerdy, M. Dantus, R. M. Bowman, and A. H. Zewail, *ibid.* **171**, 1 (1990).

[7] N. F. Scherer, L. D. Ziegler, and G. R. Fleming, J. Chem. Phys. (in press).

[8] S. Ruhman, A. G. Joly, B. Kohler, L. R. Williams, and K. A. Nelson, Rev. Phys. Appl. **22**, 1717 (1987); S. Ruhman, A. G. Joly, and K. A. Nelson, IEEE J. Quantum Electron. **QE-24**, 460 (1988).

[9] D. M. McMorrow, W. T. Lotshaw, and G. A. Kenny-Wallace, IEEE J. Quantum Electron. **QE-24**, 443 (1988).

[10] J. Y. Bigot, M. T. Portella, R. W. Schoenlein, C. J. Bardeen, A. Migus, and C. V. Shank, Phys. Rev. Lett. **66**, 1138 (1991).

[11] E. T. Nibbering, D. A. Wiersma, and K. Duppen, Phys. Rev. Lett. **66**, 2464 (1991).

[12] S. Mukamel, Ann. Rev. Phys. Chem. **41**, 647 (1990).

[13] W. T. Pollard, S.-Y. Lee, and R. A. Mathies, J. Chem. Phys. **92**, 4012 (1990).

[14] A. Villaeys and K. F. Freed, Chem. Phys. **13**, 271 (1976).

[15] H. Metiu and V. Engel, J. Opt. Soc. Am. B **7**, 1709 (1990); V. Engel and H. Metiu (unpublished manuscript).

[16] D. J. Tannor and S. A. Rice, J. Chem. Phys. **83**, 5013 (1985) [see especially the paragraph preceding Eq. (11)]; Adv. Chem. Phys. **70**, 441 (1988); D. J. Tannor, R. Kosloff, and S. A. Rice, J. Chem. Phys. **85**, 5805 (1986).

[17] J. A. Cina, Phys. Rev. Lett. **66**, 1146 (1991); J. A. Cina and V. Romero-Rochin, J. Chem. Phys. **93**, 3844 (1990); V. Romero-Rochin and J. A. Cina, *ibid.* **91**, 6103 (1989); J. A. Cina, T. J. Smith, Jr., and V. Romero-Rochin, Adv. Chem. Phys. (in press).

[18] R. G. Gordon, Adv. Mag. Reson. **3**, 1, (1968).

[19] E. J. Heller, Acc. Chem. Res. **14**, 368 (1981).

[20] R. D. Coalson, J. Chem. Phys. **94**, 1114 (1991).

[21] X.-P. Jiang, R. Heather, and H. Metiu, J. Chem. Phys. **90**, 2555 (1989).

[22] S. L. Tang, D. G. Imre, and D. Tannor, J. Chem. Phys. **92**, 5919 (1990).

[23] R. Bavli, E. Engel, and H. Metiu, J. Chem. Phys. (in press).

[24] N. F. Scherer, M. Du, A. Ruggiero, H. Guttman, and G. R. Fleming (in preparation).

[25] A. Ruggiero, N. F. Scherer, G. M. Mitchel, G. R. Fleming, and J. Hogan, J. Opt. Soc. Am. B **8**, 2061 (1991).

[26] A. Ruggiero, N. F. Scherer, and G. R. Fleming (in preparation).

[27] G. Herzberg, *Spectra of Diatomic Molecules*, 2nd ed. (Van Nostrand Reinhold, New York, 1950).

[28] L. D. Landau and E. M. Lifschitz, *Statistical Physics* (Pergamon, New York, 1980), Part I, Ch. XII.

[29] E. J. Heller, J. Chem. Phys. **68**, 2066 (1978).

[30] R. G. Brewer and R. L. Shoemaker, Phys. Rev. A **7**, 2105 (1973); R. G. Brewer and A. Genack, Phys. Rev. Lett. **36**, 959 (1976).

[31] J. Tellinghuisen, J. Quantum Spectrosc. Radiative Trans. **19**, 149 (1978).

[32] R. J. LeRoy, J. Chem. Phys. **52**, 2678 (1969).

[33] R. F. Barrow and K. K. Yee, J. Chem. Soc. Faraday Trans. 2 **69**, 684 (1973).

[34] G. V. Hartland, L. L. Connell, and P. M. Felker, J. Chem. Phys. **94**, 7649 (1991).

[35] J. Tellinghuisen, J. Chem. Phys. **76**, 4736 (1982).

[36] S. Gerstenkorn and P. Luc, *Atlas Du Spectre D'Absorption De La Molecule D'Iode* (Centre National de la Recherche Scentifique, Paris, 1978).

[37] Calculations were performed with a 2.5 nm shift to 618.5 nm for the detection window. The results of Fig. 9 required only a 0.5 nm shift. Other spectrally windowed experiments were also best simulated with a 0.5 nm shift. Apparently the wavelength reading for the data set of Fig. 10 was in error by 2 nm and we believe (from comparison with other data not shown) the correct value to be 618 nm. The data set was chosen for the figure because it best illustrates the windowing effect on the interferogram.

[38] A. Matro, L. W. Ungar, N. F. Scherer, J. A. Cina, and G. R. Fleming (unpublished results).

[39] E. T. Sleva and A. H. Zewail, Chem. Phys. Lett. **110**, 582 (1984).

[40] R. A. Harris, R. A. Mathies, and W. T. Pollard, J. Chem. Phys. **85**, 3744 (1986).

[41] Y. J. Yan, L. E. Fried, and S. Mukamel, J. Phys. Chem. **93**, 8149 (1989).